Eurasian Chem.-Technol. J. 28 (2026) 171–179
The journal of the Institute of Combustion Problems https://ect-journal.kz

https://doi.org/10.18321/ectj1692

Optimization of Deposition and Properties of Printed Complex-Composition Perovskite Films for Flexible Solar Cells

Yerassyl Yerlanuly[1,2]* and Askhat Jumabekov[1,2]

[1]National Laboratory Astana, Kabanbay Batyr Ave. 53, Astana, Kazakhstan
[2]Department of Physics, School of Sciences and Humanities, Nazarbayev University, Kabanbay Batyr Ave. 53, Astana, Kazakhstan

Article info

Received:
13 February 2026

Received in revised form:
26 April 2026

Accepted:
10 June 2026

Keywords:
Printed perovskite solar cells
Flexible photovoltaics
Slot-die coating
Mixed-cation perovskites
Crystallization additives

Abstract

Scalable deposition of high-quality perovskite films is a key challenge for the commercialization of flexible perovskite solar cells. In this work, the deposition process and material properties of printed mixed-cation, mixed-halide perovskite films with the composition $Cs_{0.175}FA_{0.75}MA_{0.075}Pb(I_{0.88}Br_{0.12})_3$ were systematically optimized using slot-die printing techniques. The influence of key printing parameters, including ink flow rate, coating speed, and substrate temperature, on film thickness, morphology, crystallization behavior, and optical properties was investigated. Optimized conditions enabled the formation of uniform perovskite layers with a thickness of 300–400 nm, a dense microstructure, and strong optical absorption with a bandgap of approximately 1.55 eV. The effects of solvent engineering and crystallization additives were further evaluated. While the pristine DMSO-based formulation provided structurally high-quality films, the incorporation of 5 mol% methylammonium chloride (MACl) significantly improved the film morphology, grain connectivity, and reproducibility without altering phase purity. Consequently, printed flexible perovskite solar cells fabricated with MACl exhibited enhanced short-circuit current density, fill factor, and power conversion efficiency (PCE), reaching a best PCE of 9.72%. These results demonstrate an effective strategy for controlling perovskite film formation in fully printed flexible devices and highlight the potential of MACl-assisted slot-die printing for flexible perovskite photovoltaics.

1. Introduction

Hybrid organic–inorganic perovskites have revolutionized the field of photovoltaics over the past decade, demonstrating an unprecedented increase in power conversion efficiency (PCE) from 3.8% to over 27% [1–4]. Their outstanding optoelectronic properties, including a high absorption coefficient, long charge-carrier diffusion lengths, and a tunable bandgap, make them highly attractive candidates for next-generation photovoltaic technologies [5–7]. In particular, mixed-cation perovskite compositions (e.g., cesium/formamidinium/methylammonium (Cs/FA/MA)) have attracted significant attention due to their enhanced thermal and phase stability compared to single-cation perovskites, leading to improved device stability and performance [8–10].

For the commercialization of perovskite photovoltaics, the development of scalable, cost-effective, and material-efficient film deposition techniques is of critical importance [11–13]. Slot-die coating has emerged as a promising approach owing to its precise material deposition, minimal waste, and compatibility with flexible substrates and patterned device architectures [14, 15]. Despite these advan-

*Corresponding author.
E-mail address: yerassyl.yerlanuly@nu.edu.kz

tages, achieving precise control over film morphology, crystallization dynamics, and thickness during printing remains challenging, as these characteristics are strongly influenced by ink rheology, printing parameters, and post-deposition processing conditions [16, 17].

In this work, we present a systematic optimization of slot-die coating for complex-composition perovskite films with the formulation $Cs_{0.175}FA_{0.75}MA_{0.075}Pb(I_{0.88}Br_{0.12})_3$, where FA and MA denote formamidinium and methylammonium cations, respectively, previously reported in the literature [18]. Particular emphasis is placed on elucidating the effects of key printing parameters, including ink flow rate, coating speed, and substrate temperature, on film thickness and morphology. In addition, the role of methylammonium chloride (MACl) as a crystallization additive is investigated with respect to film quality and structural stability. Based on the optimized printing conditions, flexible perovskite solar cells (FPSCs) were fabricated and comprehensively characterized, demonstrating the viability of the proposed approach for scalable flexible photovoltaic devices.

2. Materials and Methods

2.1. Materials

All the chemicals were used as received without further purification. Indium tin oxide-coated polyethylene terephthalate (PET/ITO) substrates (thickness: 125 μm, sheet resistance: 45 Ω/sq) were obtained from Mekoprint. Tin(IV) oxide colloidal nanoparticle solution (SnO_2, 15 wt.% in H_2O colloidal dispersion) was purchased from Alfa Aesar. Lead iodide (PbI_2, 99%), lead bromide ($PbBr_2$, 99.999%), bis(trifluoromethane)sulfonimide lithium salt (Li-TFSI, 99%), 4-tert-Butylpyridine (4-tBP, 98%), cesium iodide (CsI, 99.999%), chlorobenzene (CB, 99.80%), acetone (99.80%), and dimethyl sulfoxide (DMSO) were obtained from Merck. N-methyl-2-pyrrolidone (NMP, 99.5%) was obtained from Thermo Scientific. Methylammonium iodide (MAI, 99.995%), formamidinium iodide (FAI, >99.99%), and methylammonium chloride (MACl, >99.99%) were obtained from GreatCell Energy. 2-Propanol (IPA, 99.80%) was obtained from a local supplier. 2,2',7,7'-Tetrakis-(N,N-di-4-methoxyphenylamino)-9,9'-spirobifluorene (Spiro-MeOTAD, 99.50%) was obtained from Lumtec. Aluminum (Al, 99.99%) and molybdenum oxide (MoO_3, 99.95%) were obtained from Kurt J. Lesker.

2.2. Preparation of perovskite ink

The base perovskite ink was prepared by dissolving stoichiometric amounts of PbI_2, $PbBr_2$, FAI, methylammonium bromide (MABr), MAI, and CsI in anhydrous DMSO to obtain a 1.4 M solution with the target composition $Cs_{0.175}FA_{0.75}MA_{0.075}Pb(I_{0.88}Br_{0.12})_3$, following the protocol described in Ref. [18]. To modify the composition 5 mol% of MACl was added to the base solution. The solutions were filtered through a 0.45 μm hydrophobic filter before use.

2.3. Device fabrication

To fabricate printed FPSCs, PET/ITO substrates were cleaned by sequential ultrasonication in deionized (DI) water with detergent, deionized (DI) water, acetone, and IPA for 10 min each. Following cleaning, the substrates were dried with a nitrogen stream and treated with UV-ozone for 15 min to enhance surface wettability. All functional layers were deposited using a slot-die coater (VectorSC or NanoRoll, FOM Technologies, Denmark). The SnO_2 electron transport layer (ETL) was prepared by diluting a commercial SnO_2 nanoparticle (NP) colloidal dispersion with DI water at a 1:3 volume ratio. The SnO_2 layer was printed at a pump rate (PR) of 150 μL/min and a chuck speed (CS) of 80 cm/min at 50 °C chuck temperature (T_c), followed by annealing at 130 °C for 30 minutes. Finally, a second 30-minute UV-ozone treatment was applied to optimize film quality and interfacial properties.

Perovskite films were deposited by slot-die coating onto freshly prepared SnO_2 ETL on PET/ITO. The printing process was carried out using a VectorSC or NanoRoll slot-die coater. The key variable parameters were the PR (10–60 μL/min), the CS (5–12 cm/min), and the T_c (25–130 °C). Immediately after printing, the samples were annealed at 100 °C for 10 minutes.

The hole transport layer (HTL) precursor was prepared by dissolving 45 mg of Spiro-OMeTAD, 28.8 μL of 4-tBP, and 17.5 μL of Li-TFSI solution (520 mg/mL in acetonitrile (ACN)) in 1 mL of CB, followed by stirring for 1 hour. The Spiro-OMeTAD layer was deposited by slot-die coating at a PR of 150 μL/min, a CS of 80 cm/min, and a T_c of 25 °C. All three functional layers were printed under ambient conditions, with the temperature and relative humidity maintained at 18–21 °C and 27–33%, respectively. The coating window (CW), defined as the distance between the shim and the substrate surface, was varied between 0.1 and 0.2 mm in all coating experiments.

Finally, a MoO_3/Al top contact was deposited using thermal evaporation (Angstrom Engineering Inc., Kitchener, Canada) at a base pressure of 2×10^{-6} Torr. The deposition rates were maintained at 0.5 Å/s for MoO_3 and 0.1 Å/s for Al, achieving optimized thicknesses of 35/100 nm for the respective layers.

2.4. Materials characterizations and device measurements

The surface morphology of the perovskite films and cross-sectional images of the device layers were obtained using a scanning electron microscope (SEM, Crossbeam 540, Zeiss, Germany). A ultraviolet–visible (UV-VIS) spectrometer (Lambda 1050, PerkinElmer, USA) was used to analyze the optical properties of the thin films. X-ray diffraction (XRD) analysis (Rigaku Smartlab, Japan) analysis was used to study the structural properties of perovskite layers. The sheet resistance of the electrodes was measured using a four-point probe system (RM3000, Jandel, UK). A semiconductor device analyzer (B1500A, Keysight, USA) coupled with a 3A+ solar simulator (Oriel Sol3A, Newport, USA) providing Air Mass 1.5 Global (AM 1.5G) illumination with an intensity of 100 mW/cm^2 was used to measure the current density–voltage (J–V) characteristics of the devices. All characterization and photovoltaic measurements were performed using instruments calibrated according to the manufacturers' procedures and standard laboratory protocols prior to data acquisition.

3. Results and Discussion

3.1. Optimization of basic printing parameters

Experiments were performed using a complex perovskite precursor solution with a concentration of 1.4 M and a composition of $Cs_{0.175}FA_{0.75}MA_{0.075}Pb(I_{0.88}Br_{0.12})_3$ dissolved in 1 mL of DMSO, following the procedure reported in [18]. The perovskite ink was deposited onto glass substrates by printing. A distinctive feature of this deposition approach is the absence of an air-knife–assisted drying step; instead, film formation and crystallization are driven by the elevated temperature of the chuck of the VectorSC slot-die coater during printing. Figure 1 presents photographs of the printed perovskite films along with the corresponding processing parameters. Based on visual inspection of the deposited layers, samples 4, 5, 7, and 8 exhibited the highest film uniformity and surface coverage, indicating that these parameter sets are optimal for producing high-quality perovskite films.

The thickness of the printed perovskite films was systematically evaluated using a stylus profilometer, and the results are presented in Fig. 2. As evidenced by the statistical analysis, the average film thickness for the investigated samples lies in the range of 300 to 400 nm, with relatively narrow thickness distributions for the optimized printing conditions This thickness range is consistent with values commonly reported for efficient perovskite optoelectronic devices, where a balance between sufficient optical absorption and efficient charge extraction must be maintained [17–18]. Consequently, the obtained film thicknesses are well suited for the fabrication of high-performance devices in subsequent processing steps.

Figure 3 shows optical microscopy images of the perovskite films deposited under different printing parameters. The top row shows low-magnification (x10) optical microscopy images of the perovskite films, revealing detailed features of the film morphology, while the bottom row provides high-magnification (x50) optical microscopy images, offering insight into the overall grain organization and uniformity in the films.

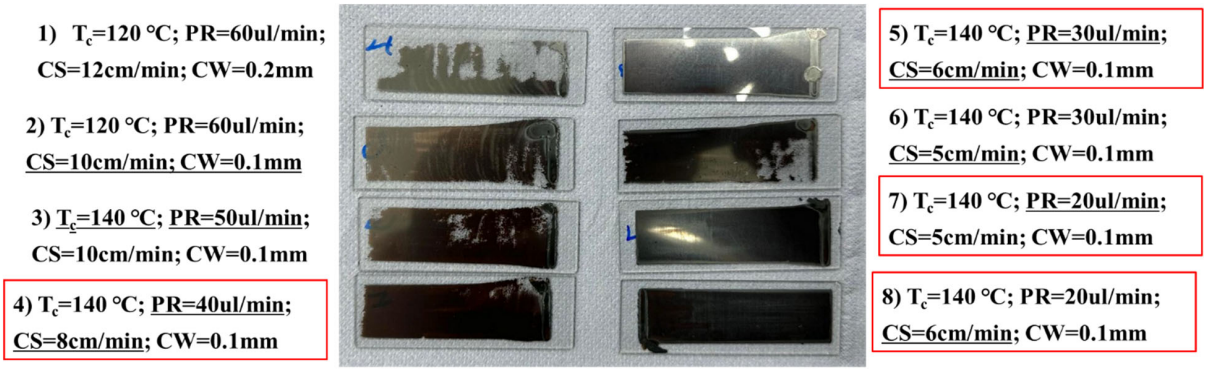

Fig. 1. Photographic images of $Cs_{0.175}FA_{0.75}MA_{0.075}Pb(I_{0.88}Br_{0.12})_3$ perovskite films on glass printed at various printing parameters.

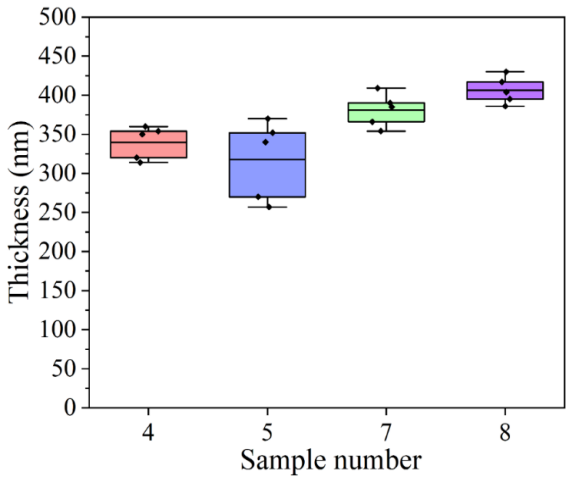

Fig. 2. Estimated thickness of the printed perovskite films on glass.

The perovskite layers exhibit a dense and continuous microstructure characterized by well-defined grain boundaries and pronounced radially oriented crystalline domains, which are particularly evident in the lower-magnification images. Variations in grain size, boundary sharpness, and domain uniformity are observed among the samples, reflecting the influence of the printing parameters on nucleation and crystal growth dynamics. Such microstructural features are known to play a critical role in carrier transport, recombination behavior, and overall device performance, indicating that optimized printing conditions promote the formation of high-quality perovskite films suitable for subsequent device fabrication.

Figure 3 shows optical microscopy images of the perovskite films deposited under different printing parameters. The top row shows low-magnification (x10) optical microscopy images of the perovskite films, revealing detailed features of the film morphology, while the bottom row provides high-magnification (x50) optical microscopy images, offering insight into the overall grain organization and uniformity in the films.

The perovskite layers exhibit a dense and continuous microstructure characterized by well-defined grain boundaries and pronounced radially oriented crystalline domains, which are particularly evident in the lower-magnification images. Variations in grain size, boundary sharpness, and domain uniformity are observed among the samples, reflecting the influence of the printing parameters on nucleation and crystal growth dynamics. Such microstructural features are known to play a critical role in carrier transport, recombination behavior, and overall device performance, indicating that optimized printing conditions promote the formation of high-quality perovskite films suitable for subsequent device fabrication.

Figure 4 presents the UV–Vis absorbance spectra of the perovskite films corresponding to samples 4, 5, 7, and 8 and measured in the wavelength range of 300–800 nm. A clear dependence of optical absorption on the printing parameters is observed. Among the investigated samples, sample 4 exhibits the lowest absorbance over the entire spectral range, whereas sample 8 shows the highest absorbance, indicating improved light-harvesting capability. Samples 5 and 7 display intermediate absorption intensities.

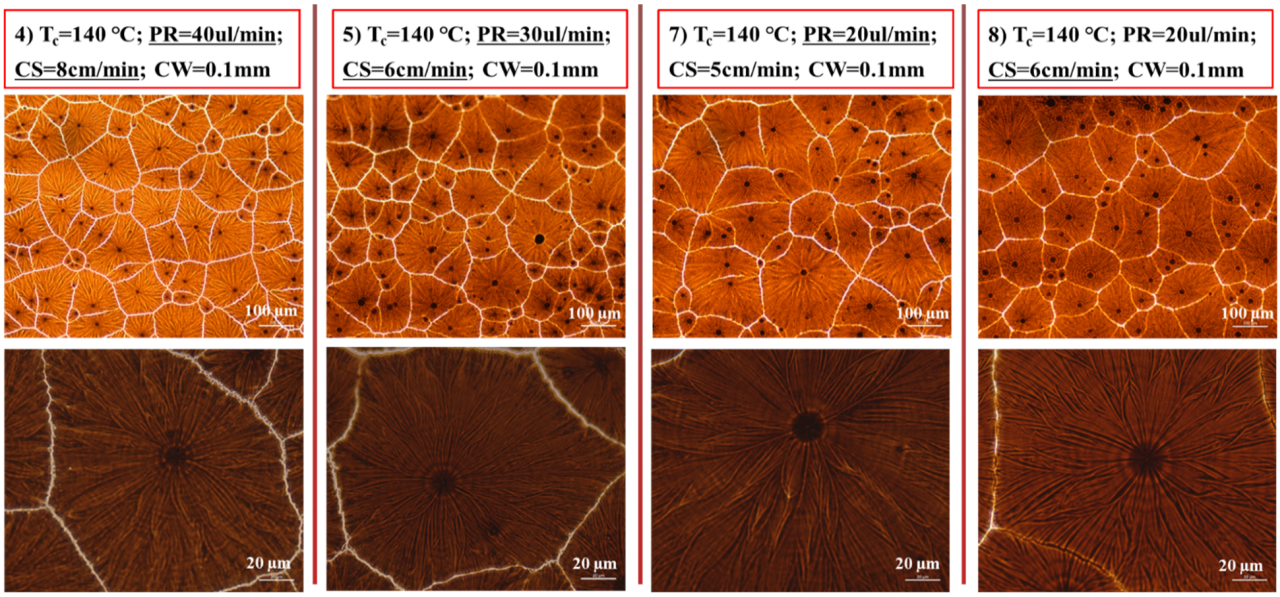

Fig. 3. Optical microscopy images of printed perovskite films on glass.

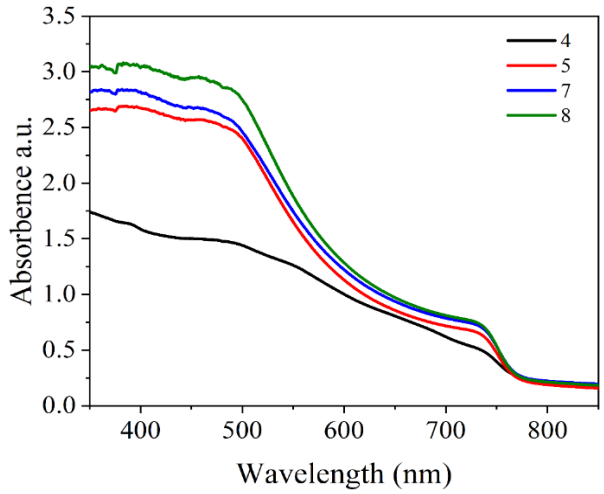

Fig. 4. Absorbance spectra of the printed perovskite films on glass.

All films exhibit a pronounced absorption onset in the range of 750–800 nm, which is characteristic to mixed-cation, mixed-halide perovskites with an optical bandgap of approximately 1.55 eV. This confirms the successful formation of the targeted perovskite phase and its suitability for optoelectronic applications. The enhanced absorbance observed for sample 8 is likely associated with its optimized film thickness and improved microstructural uniformity, suggesting that this sample is particularly promising for high-performance device fabrication.

Experiments using a complex perovskite solution (1.4 M $Cs_{0.175}FA_{0.75}MA_{0.075}Pb(I_{0.88}Br_{0.12})_3$ in DMSO) on glass substrates showed that crystallization, driven by high substrate temperatures, produces films with excellent uniformity under specific conditions. Analysis of the films revealed an optimal thickness range of 300–400 nm and demonstrated superior optical properties, particularly in samples formed under the best conditions, such as sample 8, which exhibited the highest absorbance. These findings establish a solid foundation for the further development of efficient and high-performance perovskite-based devices.

Although the conducted experiments successfully determined the optimal parameters for the deposition of high-quality perovskite films and demonstrated promising optical and structural properties, further studies and experiments are required. Additional investigations are needed to refine the deposition process, explore the long-term stability of the films, and evaluate their performance under various environmental and operational conditions. Moreover, experiments on scaling up the fabrication process and integrating these films into complete device structures are essential for advancing towards practical applications. These further studies will help ensure the reliability and efficiency of perovskite-based devices in real-world scenarios.

3.2. Effect of MACl additive

To further improve the structural quality of the perovskite films and suppress intergranular voids, 5 mol% methylammonium chloride (MACl) was incorporated into the perovskite precursor composition as a crystallization modulator. In this study, 5 mol% MACl was selected based on previous reports demonstrating that low MACl concentrations effectively modulate crystallization and improve film morphology while preserving phase purity [16, 17]. Figure 5 shows top-view scanning electron microscopy (SEM) images of the printed perovskite films fabricated at different coating speeds. At relatively low coating speeds, the films exhibit compact microstructures with well-connected grains and minimal intergranular gaps, indicating effective crystal growth and coalescence promoted by the addition of MACl.

With increasing coating speed, a progressive degradation of film morphology is observed, manifested by the appearance of cracks and enlarged grain boundaries between adjacent perovskite domains. This behavior can be attributed to accelerated solvent evaporation and reduced time for crystal rearrangement and grain fusion during film formation. Furthermore, cross-sectional SEM images (Fig. 6) reveal a monotonic decrease in film thickness with increasing coating speed, which is consistent with the reduced material deposition per unit area at higher speeds.

These results demonstrate that although MACl additive effectively enhances crystallization and improves film continuity under optimized printing conditions, excessively high coating speeds adversely affect the film uniformity and structural integrity. Therefore, careful optimization of the coating speed is essential to fully exploit the beneficial role of MACl additive and to achieve high-quality perovskite films suitable for subsequent device fabrication.

Figure 7 shows the X-ray diffraction (XRD) patterns of the printed perovskite films on glass with MACl additive and deposited at different coating speeds. All samples exhibit well-defined diffraction peaks characteristic of the perovskite crystal structure, confirming the formation of a single-phase perovskite without detectable secondary phases over the investigated range of coating speeds. The dominant reflections can be indexed to the (100), (110), (111), (200), (210), (211), (220), and (300) planes, indicating preservation of the tetragonal perovskite lattice.

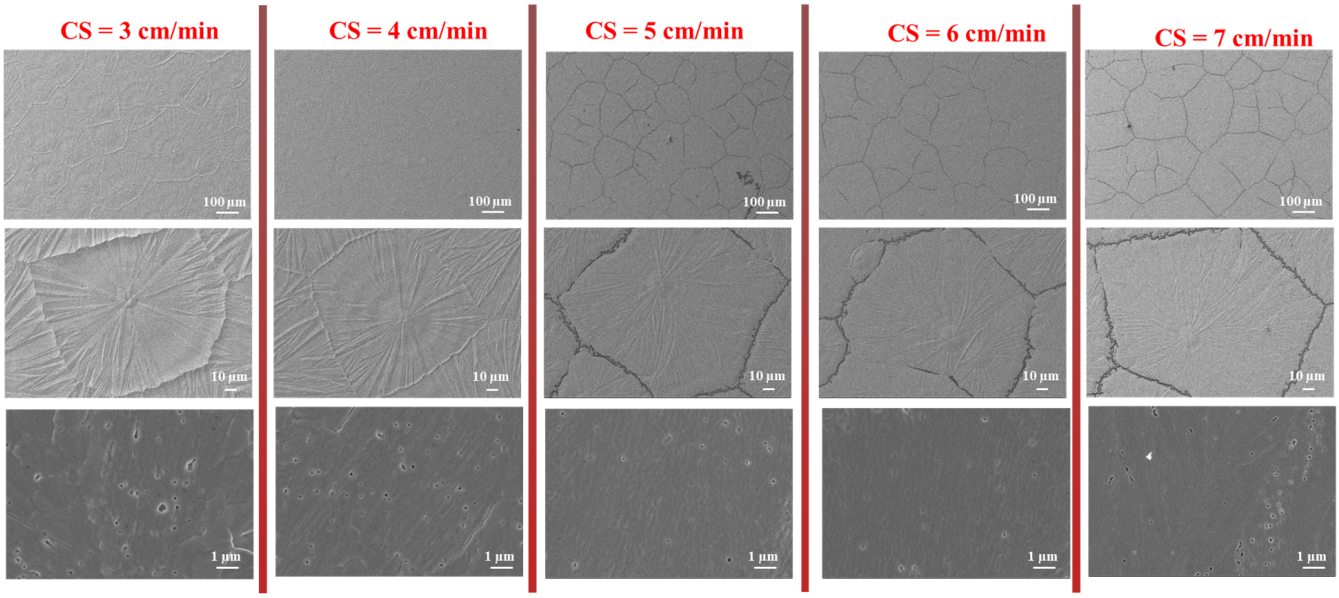

Fig. 5. Top-view SEM images of printed perovskite films on glass with MACl additive.

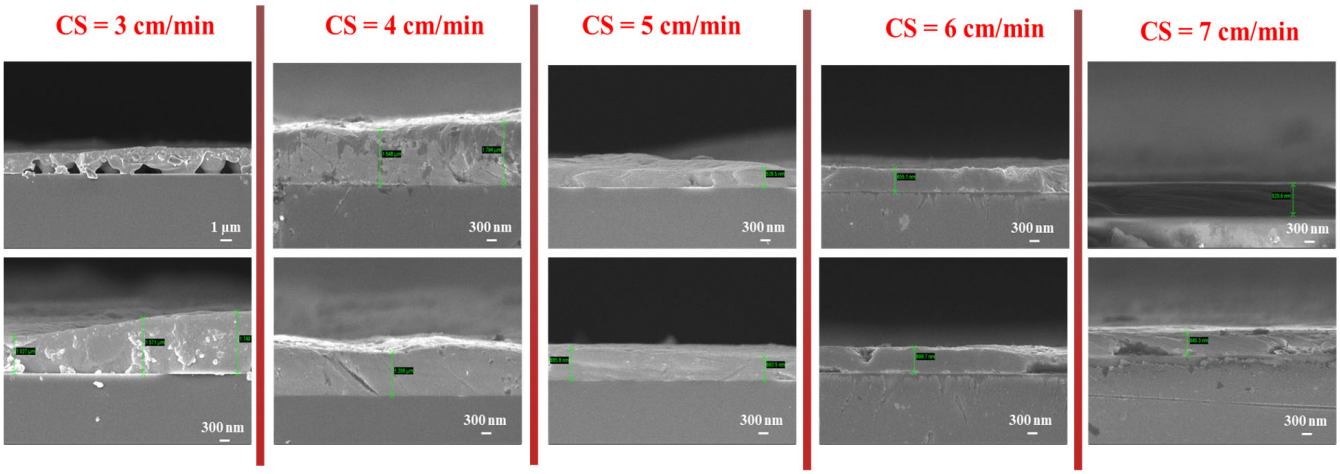

Fig. 6. Cross-sectional SEM images of printed perovskite films on glass with MACl additive.

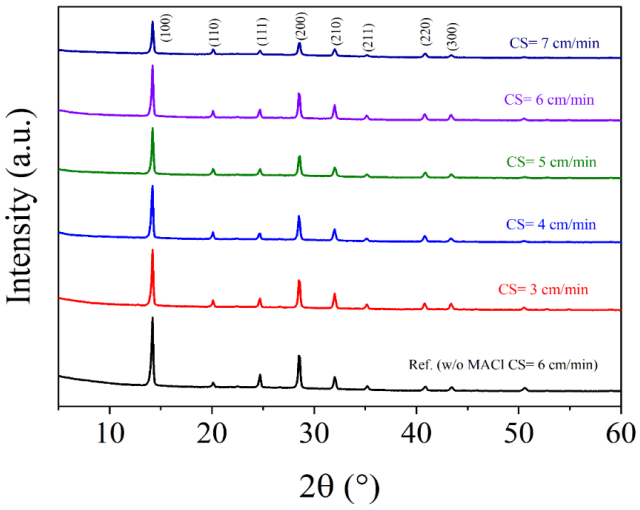

Fig. 7. XRD patterns of printed perovskite films on glass with MACl additive.

A comparison of the diffraction patterns reveals no noticeable peak shifts or additional reflections with increasing coating speed, suggesting that variations in deposition speed do not induce changes in lattice parameters or phase composition. Minor variations in peak intensity can be attributed to differences in film thickness and preferred crystallographic orientation rather than structural changes. Importantly, the MACl-containing films exhibit diffraction features comparable to those of the reference sample prepared without MACl addition. This indicates that MACl acts as a crystallization additive without altering the intrinsic perovskite crystal structure. Overall, the XRD results demonstrate that the incorporation of MACl ensures phase stability of the perovskite films across a broad range of coating speeds, highlighting the structural tolerance of the optimized printing process.

3.3. Fabrication and characterization of flexible perovskite solar cells

Subsequently, printed flexible perovskite solar cells (FPSCs) were fabricated using the optimized perovskite ink, and their photovoltaic performance was evaluated. Figure 8 summarizes the device structure and statistical analysis of the key photovoltaic parameters for reference devices and devices incorporating MACl. The statistical analysis was performed based on 70 devices for each condition. As shown in Fig. 8a, the FPSCs adopt a conventional n–i–p architecture consisting of PET/ITO/SnO_2/perovskite ($Cs_{0.175}FA_{0.75}MA_{0.075}Pb(I_{0.88}Br_{0.12})_3$)/Spiro-OMeTAD/$MoO_3$/Al.

The J–V characteristics of the best-performing devices measured under reverse scan (RS) and forward scan (FS) conditions are shown in Fig. 8b. For both the reference and MACl-containing devices, the RS measurements consistently exhibit higher current densities than the FS measurements, indicating scan-direction-dependent hysteresis. Notably, the devices incorporating MACl demonstrate superior J–V characteristics in both scanning directions, with enhanced current density and improved curve squareness compared to the reference devices.

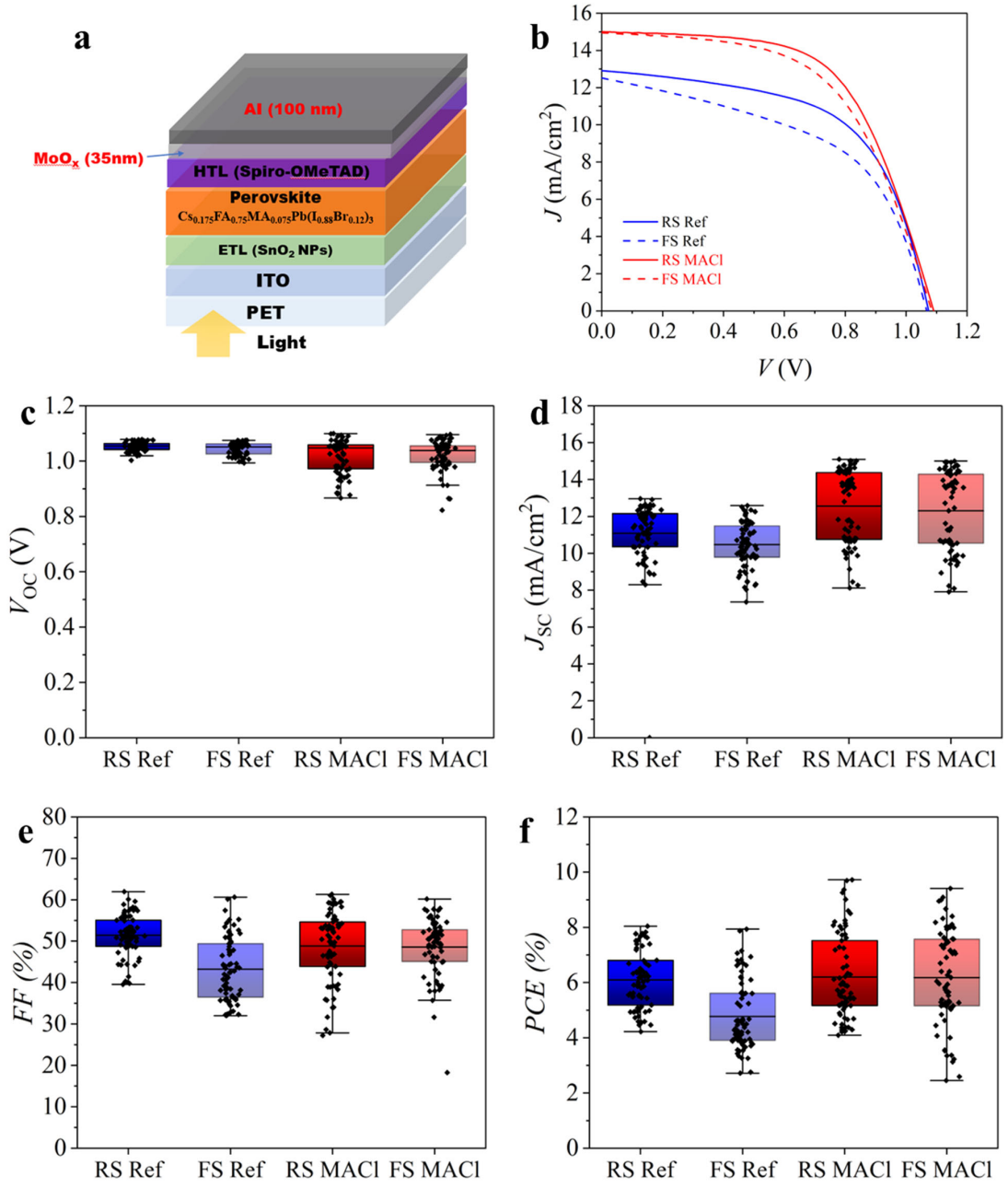

Fig. 8. Device structure (a) and J–V curves (b) of printed FPSCs; c) J_{SC}, d) V_{OC}, e) FF, and f) PCE of printed FPSCs with and without MACl additive.

Under reverse scan conditions, the reference device exhibits an open-circuit voltage (V_{OC}) of 1.074 V, a short-circuit current density (J_{SC}) of 12.91 mA/cm^2, a fill factor (FF) of 58.0%, and a PCE of 8.04%. In contrast, the MACl-containing device delivers a higher V_{OC} of 1.091 V, a significantly increased J_{SC} of 15.01 mA/cm^2, an improved FF of 59.4%, and a substantially enhanced PCE of 9.72%.

The pronounced improvement in J_{SC} and FF upon MACl incorporation directly translates into a notable enhancement in overall device efficiency. This performance enhancement is attributed to the improved structural quality and morphology of the perovskite films induced by MACl, including reduced defect density, improved grain connectivity, and more efficient charge transport and collection.

Figures 8c and 8d show the statistical distributions of V_{OC} and J_{SC}, respectively. The V_{OC} values remain relatively unchanged upon MACl incorporation, suggesting that the additive does not significantly affect the energetic alignment between the device functional layers. In contrast, a clear increase in J_{SC} is observed for MACl-containing devices in both reverse-scan (RS) and forward-scan (FS) modes, which can be attributed to improved film morphology, reduced defect density, and enhanced charge collection efficiency.

Figures 8e and 8f present the statistical distributions of FF and PCE, respectively. Devices incorporating MACl exhibit higher and more reproducible FF values compared to the reference devices, indicating reduced series resistance and improved charge transport across the interfaces. As a direct consequence of the enhanced JSC and FF, the MACl-containing devices demonstrate a systematic improvement in PCE under both scanning directions.

Overall, the results establish a clear process–structure–property–performance relationship: printing parameters such as flow rate, coating speed, and substrate temperature govern solvent evaporation and crystallization kinetics; which in turn determine film thickness, grain connectivity, and surface uniformity. The resulting structural and optical properties influence charge transport and recombination losses, ultimately controlling the photovoltaic parameters of the flexible solar cells. In particular, MACl-assisted printing improves grain connectivity and reduces morphological defects, which is reflected in enhanced J_{SC}, FF, and PCE.

4. Conclusion

In conclusion, uniform mixed-cation, mixed-halide perovskite films were successfully fabricated by slot-die printing through optimization of flow rate, coating speed, substrate temperature, and ink formulation. The optimized process enabled the formation of perovskite layers with favorable thickness, dense morphology, preserved crystal structure, and strong optical absorption. Within this flexible device architecture, the incorporation of MACl improved grain connectivity and film reproducibility, leading to enhanced short-circuit current density, fill factor, and overall power conversion efficiency. These results highlight the importance of process control in determining film structure and device performance, and demonstrate the practical potential of MACl-assisted slot-die printing for scalable flexible perovskite photovoltaics.

Acknowledgments

This research was funded by the Science Committee of the Ministry of Science and Higher Education of the Republic of Kazakhstan (Grant No. AP26194151).

References

[1]. Z. Xiong, Q. Zhang, K. Cai, H. Zhou, Q. Song, et al., Homogenized chlorine distribution for >27% power conversion efficiency in perovskite solar cells, *Science* 390 (2025) 638–642. DOI: 10.1126/science.adw8780

[2]. National Laboratory of the Rockies. Best Research-Cell Efficiency Chart. Available at: NREL website: https://www.nlr.gov/pv/cell-efficiency

[3]. P. Phonglamjiakngam, Z.A.M. Hazaea, M. Wang, N. Pootrakulchote, Recent progress on raising the efficiency of lead free double perovskite solar cells, *Solar Energy* 303 (2026) 114164. DOI: 10.1016/j.solener.2025.114164

[4]. W. Gao, F. Yang, Z. Wang, Y. Lan, R. Nie, C. Ran, Interface Matters: Boosting Efficient Pb-Sn Perovskite Solar Cells for All-Perovskite Tandem Photovoltaics, *Adv. Mater*. 38 (2026) e21789. DOI: 10.1002/adma.202521789

[5]. J.J. Yoo, G. Seo, M.R. Chua, T.G. Park, Y. Lu, et al., Efficient perovskite solar cells via improved carrier management, *Nature* 590 (2021) 587–593. DOI: 10.1038/s41586-021-03285-w

[6]. W. Zhou, Y. Fang, C. Zhang, M. Xie, T. Geng, et al., A comprehensive review of hole-transporting materials for inverted perovskite solar cells, *Sol. Energy Mater. Sol. Cells* 296 (2026) 114079. DOI: 10.1016/j.solmat.2025.114079

[7]. J. Han, K. Park, S. Tan, Y. Vaynzof, J. Xue, et al., Perovskite solar cells, *Nat. Rev. Methods Primers* 5 (2025) 3. DOI: 10.1038/s43586-024-00373-9

[8]. M. Saliba, T. Matsui, J.-Y. Seo, K. Domanski, J.-P. Correa-Baena, et al., Cesium-containing triple cation perovskite solar cells: improved stability, reproducibility and high efficiency, *Energy Environ. Sci.* 9 (2016) 1989–1997. DOI: 10.1039/C5EE03874J

[9]. L.J. Diguna, A. Lim, Y. Firdaus, L.J. Widiapradja, D.H. Sidiq, et al., The role of perovskite composition, dimensionality, and additives in lead-free perovskite solar cell longevity: a review, *Sustain. Energy Fuels* 9 (2025) 6413–6438. DOI: 10.1039/D5SE00738K

[10]. J. Zhang, J. Fu, K. Wang, C. Zhang, Y. Wang, et al., Performance promotion strategies for wide bandgap perovskite solar cells, *Sustain Energy Fuels* 9 (2025) 303–322. DOI: 10.1039/D4SE00433G

[11]. N. Mussakhanuly, Y. Yerlanuly, H.P. Parkhomenko, A. Niyetullayeva, A.K. Azamat, et al., Laminated Carbon Based Flexible Printed Perovskite Solar Cells Passivated with Tin(II) Phthalocyanine, *Adv. Mater. Interfaces* 12 (2025) 2400591. DOI: 10.1002/admi.202400591

[12]. Y. Yerlanuly, E.O. Shalenov, H.P. Parkhomenko, M.S. Kiani, Z. Kukhayeva, et al., Elucidating the hysteresis effect in printed flexible perovskite solar cells with SnO2 quantum dot- and PCBM-based electron transport layers, *Heliyon* 10 (2024) e39667. DOI: 10.1016/j.heliyon.2024.e39667

[13]. H.P. Parkhomenko, Y. Yerlanuly, V.V. Brus, A.N. Jumabekov, Effect of mild mechanical stresses on device physics of slot-die coated flexible perovskite solar cells, *Org. Electron*. 129 (2024) 107049. DOI: 10.1016/j.orgel.2024.107049

[14]. R. Patidar, D. Burkitt, K. Hooper, D. Richards, T. Watson, Slot-die coating of perovskite solar cells: An overview, *Mater Today Commun.* 22 (2020) 100808. DOI: 10.1016/j.mtcomm.2019.100808

[15]. K.K. Shin Thant, C. Seriwattanachai, T. Jittham, N. Thamangraksat, P. Sakata, P. Kanjanaboos, Comprehensive Review on Slot-Die-Based Perovskite Photovoltaics: Mechanisms, Materials, Methods, and Marketability, *Adv. Energy Mater.* 15 (2025) 2403088. DOI: 10.1002/aenm.202403088

[16]. D.T. Cuzzupè, S.D. Öz, J. Ling, E. Illing, T. Seewald, et al., Understanding the Methylammonium Chloride-Assisted Crystallization for Improved Performance of Lead-Free Tin Perovskite Solar Cells, *Solar RRL* 7 (2023) 2300770. DOI: 10.1002/solr.202300770

[17]. M.G.D. Guaita, R. Szostak, F.M.C. da Silva, A. de Morais, R.F. Moral, et al., Influence of Methylammonium Chloride on Wide-Bandgap Halide Perovskites Films for Solar Cells, *Adv. Funct. Mater.* 34 (2024) 2307104. DOI: 10.1002/adfm.202307104

[18]. S.S. Sangale, S. Kwon, P. Patil, H. Lee, S. Na, Locally Supersaturated Inks for a Slot-Die Process to Enable Highly Efficient and Robust Perovskite Solar Cells, *Adv. Energy Mater.* 13 (2023) 2300537. DOI: 10.1002/aenm.202300537